Astronomy & Astrophysics manuscript no. Edese
April 22, 2024

A multigrain-multilayer astrochemical model with variable desorption energy for surface species

Juris Kalvāns, Aija Kalniņa, and Kristaps Veitners

Engineering Research Institute "Ventspils International Radio Astronomy Center" of Ventspils University of Applied Sciences, Inženieru 101, Ventspils, LV-3601, Latvia
e-mail: juris.kalvans@venta.lv

Received March 20, 2024; accepted March 16, 1997

ABSTRACT

Context. Interstellar surface chemistry is a complex process that occurs in icy layers accumulated onto grains of different sizes. Efficiency of surface processes often depends on the immediate environment of adsorbed molecules.
Aims. We investigate how gas-grain chemistry changes when surface molecule desorption is made explicitly dependent to the molecular binding energy, which is modified, depending on the properties of the surface.
Methods. Molecular binding energy changes gradually for three different environments – bare grain, where polar, water-dominated ices and non-polar, carbon monoxide-dominated ices. In addition to diffusion, evaporation and chemical desorption, photodesorption was also made binding energy-dependent, in line with experimental results. These phenomena occur in a collapsing prestellar core model that considers five grain sizes with ices arranged into four layers.
Results. Efficient chemical desorption from bare grains significantly delays ice accumulation. Easier surface diffusion of molecules on non-polar ices promotes the production of carbon dioxide and other species.
Conclusions. The composition of interstellar ices is regulated by several binding-energy dependent desorption mechanisms. Their actions overlap in time and space, which explains the ubiquitous proportions of major ice components (water and carbon oxides), observed to be similar in all directions.

Key words. astrochemistry – molecular processes – methods: numerical – interstellar medium: clouds, dust – stars: formation

1. Introduction

During the last decade, theoretical astrochemists have expanded gas-grain models with additional phases of solid matter. These include reactive icy molecules residing either in different layers on interstellar grains or on grains of different sizes. In conjunction with dynamical evolution of dense cores and an improved understanding of microscopic phenomena, the new phases allow to paint a detailed picture about chemical processes in interstellar and circumstellar ices. The microscopic phenomena most notably include efficient chemical desorption and molecular desorption (binding) energy that varies depending on its surrounding environment. The above ingredients have never been combined in a single model, which means that current astrochemical models may be missing key processes that regulate ice formation and distribution between solid phases.

Multigrain models consider simultaneous surface chemistry on grains with an assortment of sizes. Acharyya et al. (2011) found that the smallest grains, having the largest overall surface, accumulate most of the ice (by default, here we consider the MRN grain size distribution of Mathis et al. 1977, used in most studies). Ice accumulation onto small grains is amplified by increase of surface area with grain growth, which is most pronounced for the small grains. Pauly & Garrod (2016); Ge et al. (2016); Iqbal & Wakelam (2018), and Chen et al. (2018) considered basic aspects for multigrain models, such as the effect of different numbers of grain size bins, the applicability of the rate-equation method, effects of differential grain temperature, and ice accumulation. A number of papers have focused on the efficiency of cosmic-ray induced desorption for grains of different sizes (Zhao et al. 2018; Sipilä et al. 2020; Kalvāns & Kalnin 2022). Some of these indicate that ices cannot efficiently accumulate on the smallest grains (Silsbee et al. 2021; Rawlings 2022). Some of the multigrain models have been applied in further astrochemical studies (Pauly & Garrod 2018; Gavino et al. 2021).

Compared to multigrain models, *multilayer* models have undergone significant evolution. They consider at least two layers of the icy mantle that cover grain surfaces (Hasegawa & Herbst 1993b), both of which may be chemically active (Kalvāns & Shmeld 2010). Current models resolve separate monolayers (MLs; Taquet et al. 2012) or up to six chemically active ice layers (Furuya et al. 2017) with limited-diffusion approaches for binary bulk-ice reactions (Chang & Herbst 2014). The mere existence of subsurface ice that is isolated from most of the desorption mechanisms acting on the exposed surface molecules is a significant development. While the chemical activity of the bulk-ice layers and their susceptibility to dissociating radiation is a matter of question, active bulk ice allows for different molecule synthesis paths, for example, in CO and H_2O-dominated environments (Chang & Herbst 2016). Moreover, multilayer models allow to regulate evaporation from ices in protostellar envelopes, either via layer-by-layer removal (Taquet et al. 2014) or by allowing hyper-volatiles to diffuse out of the mantle first (Garrod 2013a, with hyper-volatiles here we understand icy species with desorption energies E_D below about 1300 K, such as H_2, N_2, O_2, CO, CH_4).

Astrophysical importance for *variable molecular desorption energy* E_D for icy surfaces with polar (H_2O) and non-polar (CO) composition was noted early by Tielens & Hagen (1982); Sandford & Allamandola (1988); Leger (1983) and Bergin et al. (1995). The latter included this effect in an astrochemical model, albeit not in a self-consistent manner (Bergin & Langer 1997). Compared to non-polar ices, a surface covered with H_2O allows binding via dipole-dipole and dipole-induced dipole interactions, as well as the strong hydrogen bonds. Besides desorption, such bonding also affects mobility of surface species, and thus, their reactivity. Further exploration of the idea of variable E_D has been limited (He et al. 2016; Garrod et al. 2022). An aspect of the variable-E_D approach is different E_D on *bare grains* and ice-covered surfaces. The binding energies to materials similar to interstellar grains are known for a limited number of species (e.g. Vidali et al. 1991). Dual (bare grain and ice) E_D have been used in by Chang et al. (2007); Taquet et al. (2014) and Hocuk & Cazaux (2015). Unlike multilayer and multigrain models, variable-E_D effects are much less understood with no dedicated studies.

The aim of this study is to combine the above phenomena within a single model that produces reasonable results, namely, ice composition and deduce if variable E_D has astrochemically significant effects. The necessary tasks include

- developing an integrated multigrain-multilayer array system for chemical species, grain, and ice parameters;
- adapting or creating descriptions the microscopic processes, notably, variable E_D for such a model; the descriptions should allow simple inclusion in other astrochemical codes;
- investigating the significance of variable E_D in modelling results;
- exploring effects that arise from phenomena that have not yet been combined together in astrochemical models.

Reproducing the proportions of major species observed in interstellar ices has been possible with simpler codes (Ruffle & Herbst 2001; Garrod & Pauly 2011), which may have deterred the advancement, or need, for more complex models. The latter two tasks involve limited parameter space analysis and will allow to understand the basic gas-grain physico-chemical interplay in dense cloud cores with the multigrain-multilayer code. This is essential before further exploration of ice chemistry can be made with the new code.

2. Methodology

The model was developed on the basis of the modified rate-equation code with multilayer ice chemistry Alchemic-Venta from of Kalvāns (2021), which is the default reference. Some multigrain aspects have been tested in Kalvāns & Silsbee (2022). The chemical model is set in a gas parcel in a low-mass contracting prestellar dark molecular core. Below, we describe the complete model with all functionalities enabled, referenced to as Model `full` in the Results section 3.

2.1. Chemical model

Table 1 lists the initial chemical abundances, used at the start of the simulation. The cosmic-ray ionization rate ζ was calculated following Padovani et al. (2009), with model "High" spectra from Ivlev et al. (2015) and depends on hydrogen column density N_H. The ζ value obtained this way is rather high for the $10^{-17}...10^{-16}$ values typically applied in astrochemistry, hence we divide it by 4π with the justification that our typical low-mass cloud core is located far from the Galactic centre and is shielded by a parent giant molecular complex. In other words, it can be said that spatially one steradian of the core is exposed to full interstellar cosmic-ray intensity. The intensity of cosmic-ray induced photons depends on ζ and was calculated with Equation (2) of Kalvāns & Kalnin (2019). The cloud is irradiated by normal interstellar radiation intensity with G_0 of $1.7 \times 10^8\,s^{-1}cm^{-2}$, attenuated the cloud's matter with $N_H/A_V = 2.2 \times 10^{21}\,cm^{-2}$ (Zuo et al. 2021). Gas temperature T_{gas} was calculated according to Equation (2) of Kalvāns (2021). Because this equation works only when interstellar extinction A_V is below or similar to 40 mag, T_{gas} was coupled to dust temperature at higher extinctions.

Table 1. Initial chemical abundances relative to total hydrogen.

Species	X/H
H_2	0.50
He	0.090
C^+	1.4×10^{-4}
N	7.5×10^{-5}
O	3.2×10^{-4}
F	6.7×10^{-9}
Na^+	2.0×10^{-9}
Mg^+	7.0×10^{-9}
Si^+	8.0×10^{-9}
P^+	3.0×10^{-9}
S^+	8.0×10^{-8}
Cl	4.0×10^{-9}
Fe^+	3.0×10^{-9}

Neutral molecules adsorb on to grain surfaces, forming an ice layer. The sticking coefficient was taken to be unity for heavy species and calculated according to Thi et al. (2010) for the light species H and H_2. The size of a "cubic average" molecule was assumed to be 0.32 nm. When ice thickness b exceeds 1 ML, excess icy molecules are moved to bulk-ice and are sequentially ordered in three subsurface ice layers. All layers are chemically active. Icy species can be destroyed via photodissociation by interstellar and cosmic-ray induced UV photons at a rate that is equal to 0.3 times their gas-phase photodissociation rate (Kalvāns 2018; Terwisscha van Scheltinga et al. 2022). The surface diffusion energy E_{diff} was taken to be $0.50E_D$. Reactions with activation barriers proceed either by hopping across the barrier or via quantum tunneling, which is possible for H and H_2 (Hasegawa & Herbst 1993a). Chemical reaction rate coefficients were adjusted for reaction-diffusion competition (Garrod & Pauly 2011). Bulk-ice molecules react with other molecules in the same layer with an approach that assumes that they are frozen in place with a bulk-ice binding (absorption) energy equal to $3E_D$ (Kalvāns 2015). Similar methods for bulk-ice chemistry have recently gained traction (Shingledecker et al. 2019; Jin & Garrod 2020).

The model considers several desorption mechanisms, with the simplest being evaporation, which is most important for H_2. Pantaleone et al. (2021) have presented credible evidence that the reaction heat of the common H+H reaction on grains may induce desorption of an adjacent hyper-volatile icy molecule. This indirect reactive desorption mechanism was included in our model with the help of Equation (16) of Kalvāns (2015) and an efficiency parameter of $\epsilon = 0.001$ desorbed molecules per

Table 2. Additions to the reaction network.

Gas-phase reactions	k(10K)[a] , cm^3 s^{-1}	Ref.[b]
CH + CH_3OH → CH_3CHO + H	2.5E-10	1,2
C + H_2CO → CO + CH_2	6.2E-10	3
CH_3 + HCO → CH_3CHO	5.0E-11	3
Surface reactions	E_A, K	Ref.
CO + H → HCO	2500	4[c]
H_2CO + H → HCO + H_2	415	5
CH_3O + H → H_2CO + H_2	0	5
CH_2OH + H → H_2CO + H_2	0	5

[a] Rate coefficient at 10 K. [b] 1 – NIST (http://kinetics.nist.gov/kinetics/index.jsp), 2 – Johnson et al. (2000), 3 – Vasyunin et al. (2017), 4 – Garrod & Herbst (2006, OSU reactions network), 5 – Minissale et al. (2016b). [c] Reaction not added, only changed its E_A.

H+H reaction act (Duley & Williams 1993; Willacy et al. 1994, see also Takahashi & Williams 2000).

For desorption via cosmic-ray induced whole-grain heating (Hasegawa & Herbst 1993a), a law that assumes similar heating frequencies for grains of different sizes was used by Kalvāns & Silsbee (2022). Here we improve this law into an based on the exhaustive new data from Kalvāns & Kalnin (2022). Namely, the cosmic-ray induced heating frequency $f_{\rm CRD}$ is now proportional to the inverse square root of grain radius a, in addition to its dependence to N_H,

$$f_{\rm CRD}(54{\rm K}) = \frac{1.93\times10^{-11}\sqrt{0.05/a}}{A_V^{1.35}4\pi}, \quad (1)$$

where a is expressed in μm. The cooling time for the grains was taken to be similar to characteristic sublimation time of CO (Hasegawa & Herbst 1993a), which is 0.002 s for a temperature of 54 K in our model. Like ζ, $f_{\rm CRD}$ was also divided by 4π. Photodesorption and desorption of chemical reaction products are described separately in Sections 2.6 and 2.7.

The chemistry in ice layers is explicitly considered, which means that the model calculates molecular abundances for each ice layer on each grain type. The actual reaction network includes multiple similar lists of surface molecular processes for each grain type and ice layer.

2.2. Reactions network

We employ UDfA Rate12 chemical network (McElroy et al. 2013) for the gas phase and a reduced OSU database for surface reactions (Garrod et al. 2008). Following Vasyunin et al. (2017), we added gas-phase COM reactions to balance the alcohol-aldehyde chemistry (Table 2). The variable-E_D approach results in generally lower molecular binding energies and more rapid diffusion of surface species, which may overproduce CO hydrogenation products. To address this, higher, original OSU database activation energy barrier E_A of 2500 K was returned for the CO + H surface reaction. Additionally, three "unproductive", H_2-producing hydrogenation reactions of intermediate CO hydrogenation products were added, all with branching probabilities of 0.5, as suggested by Minissale et al. (2016b). The latter reactions supplement similar additions to Alchemic-Venta in Tables 4 and 6 of Kalvāns (2015). Table 2 summarizes these changes to the network.

To reduce the overall number of species and reactions, phosphorus compounds with two or more C atoms were removed.

Table 3. Dust grain radius a and number density relative to H atoms..

a μm	n_g/n_H
0.037	5.46E-12
0.058	1.73E-12
0.092	5.46E-13
0.146	1.73E-13
0.232	5.46E-14

These species are irrelevant to the overall chemistry, because of the low abundance of P, and their low abundance, even relative to simpler P species. Network reduction ensured a smooth operation of the code and reduced computing time at a little cost to the scientific output, since we do not study the chemistry of phosphorus.

2.3. Grain physics

We divide the MRN grain size distribution in five bins with logarithmic spacing. It is a compromise, which allows to model multigrain surface chemistry in significant detail, while not making the model overly complex. The number of grain size bins has a limited effect on modelling results (Iqbal & Wakelam 2018), while five bins have been used also by other authors (Acharyya et al. 2011; Pauly & Garrod 2016; Sipilä et al. 2020). Table 3 shows the assumed grain sizes and abundances.

Moreover, here we assume grains that have already undergone processing in a star-forming region, i.e., the grains have a carbonaceous coating, not unlike interplanetary dust particles (Flynn 2020). While such a choice may be physically justified, in our model it has the benefit of bare surface being significantly different from water-dominated ices. This means that the effects of an E_D that differs for bare and ice-covered grains can be more pronounced (Section 2.5). A second consequence of the processed-grain assumption is that the smallest grains must have have been depleted by sticking to larger grains (Silsbee et al. 2020); thus we adopt the sizes and relative abundances of grains from Sipilä et al. (2020). Importantly, exclusion of the small grains reduces the average temperature and reactivity of surface species, which results, for example, in lower abundances of CO_2 ice (see also Iqbal & Wakelam 2018). Therefore, grain size distribution is another aspect that regulates the calculated composition of ices, in addition to the existence of active or passive bulk ice, the $E_{\rm diff}/E_D$ ratio, reaction activation barriers, and selective desorption mechanisms. A benefit for our model is that the exclusion of the small grains allows adequate operation for the modified rate-equation procedure of the ALCHEMIC code (Semenov et al. 2010).

For calculating the cosmic-ray-induced whole-grain heating rate (see above), Kalvāns & Kalnin (2022) considered refractory grains consisting of 40 % amorphous carbon and 60 % silicates by mass. The resulting grain density was 2.6 g cm^{-3}. The grain mass obtained with this density constitutes 0.4 % of the gas mass, in contrast to 0.5 % for distributions that include smaller grains, such as Acharyya et al. (2011). We did not consider loss of grain mass; instead the small grains are stuck on to the large grains, in effect, increasing their abundance. To account for the mass gap, the Sipilä et al. (2020) grain abundances were multiplied by a factor of 1.25. An additional 0.8 % of cloud mass are in the elements heavier than He ("metals") that constitute icy mantles in freeze-out conditions (Table 1). Grains grow as the icy mantles accumulate and increase thickness. The temperature of the dust grains T_d was calculated with the method given

by Hocuk et al. (2017, for $a = 0.1\,\mu$m grains), and attributed to different grain sizes following Pauly & Garrod (2016), i.e., $T_d \propto a^{1/6}$.

2.4. Variable desorption energy

Over the years, E_D measurements and calculations have been done for various species relevant to interstellar ices. Our task here is to devise a relation that describes how E_D changes for a molecule embedded in an environment rich in polar species ($E_{D,\mathrm{pol}}$), such as H_2O, relative to the same molecule in non-polar ices, such as CO ($E_{D,\mathrm{np}}$). Thus, we are interested in measurements that directly correlate molecular E_D in polar an non-polar environments. Such measurements are possible only for volatile molecules, which evaporate first. Probably the most relevant molecule is CO itself, which is sufficiently abundant to make non-polar parts of interstellar ices (Sandford & Allamandola 1988; Tielens et al. 1991). While it is clear that the actual E_D includes a range of values, depending on the properties of individual adsorption sites and the orientation of the molecule (He et al. 2018; Grassi et al. 2020), here we employ single-value E_D, which is a standard practice in astrochemistry.

Desorption energy for CO in watery ices has been considered to be 1150 K (Collings et al. 2004; Noble et al. 2012; Penteado et al. 2017) or 1300 K (Wakelam et al. 2017; Das et al. 2018). In a pure-ice CO matrix, $E_{D,\mathrm{np,CO}}$ of CO has been measured to be 954 K by Shinoda (1969), while more recent measurements give values of 855, 858, 866, and 899 K (Öberg et al. 2005; Acharyya et al. 2007; Fayolle et al. 2016; Martín-Doménech et al. 2014, respectively). Another molecule for which data are available that help evaluating the ratio $E_{D,\mathrm{np}}/E_{D,\mathrm{pol}} \equiv np/pol$ is molecular nitrogen. In a H_2O matrix, $E_{D,\mathrm{pol,N_2}}$ has been determined to be in the range of 810–1400 K (Wakelam et al. 2017; Das et al. 2018; Penteado et al. 2017). For non-polar environments, $E_{D,\mathrm{np,N_2}}$, measurements have been made for N_2 matrices, obtaining values of 779 and 790 K (Fayolle et al. 2016; Öberg et al. 2005, respectively). These values yield a wide-ranged *np/pol* ratio of 0.56...0.98.

The procedure in our model for calculating E_D for species in ices is as follows. The original, or default E_D values are $E_{D,\mathrm{pol}}$ from the OSU surface network, replaced by those of Wakelam et al. (2017), where possible. An exception was made for the volatile CO, N_2, and CH_4 molecules, whose $E_{D,\mathrm{pol}}$ were adopted from Penteado et al. (2017). The values of $E_{D,\mathrm{pol}}$ correspond to a matrix (surface) consisting of pure water with $E_{D,\mathrm{pol,H_2O}} = 5600$ K. First, the model obtains the weighed average $\bar{E}_{D,\mathrm{pol}}$ for the whole ice phase in consideration (one of four layers on one of five types of grains), taking into account all icy species in that phase. Then we calculate *np/pol* with

$$np/pol = \frac{\bar{E}_{D,\mathrm{pol}} + (X_{\mathrm{des}} - 1)E_{D,\mathrm{pol,H_2O}}}{X_{\mathrm{des}} E_{D,\mathrm{pol,H_2O}}}\,, \tag{2}$$

and the final desorption energy for species A, used for calculating desorption and surface diffusion rates is $E_{D,\mathrm{A}}$

$$E_{D,\mathrm{A}} = E_{D,\mathrm{pol,A}} \times [np/pol]\,. \tag{3}$$

This approach adjusts species' E_D in accordance with the environment it resides in and depends only on a single external parameter $X_{\mathrm{des}} = 4.00$. This value corresponds to $np/pol \approx 0.8$. For example, $E_{D,\mathrm{CO}}$ decreases from 1150 K in a H_2O matrix environment to 922 K in a pure CO matrix. In modelled multilayer ices, where Equation (3) operates, the extreme values are never reached and the *np/pol* lies in between 0.8 and 1. Equation (3) was not applied in cases when a molecule's $E_{D,\mathrm{pol,A}}$ was already lower than the average $E_{D,\mathrm{pol}}$ in the ice layer. To avoid discontinuities in modelled abundances, variable E_D was applied proportionally to ice thickness, from 0 MLs with no effect, when icy molecules barely interact, to full effect at 2 MLs and above, when most icy molecules primarily interact with neighbouring adsorbed species, instead of the refractory grain surface.

Summarizing, Equations (2) and (3) present a simple approach for calculating E_D for a molecule in ice with changing composition and, thus, changing average desorption energy of species in this icy phase. In practice, *np/pol* is determined by a few species that dominate a given ice phase at a given time step. Most often these are H_2O, CO, CO_2, N_2, and CH_3OH.

Variable ice E_D, calculated from the abundance of H_2, has been employed also by Garrod et al. (2022). They do not apparently base their approach on experimental or theoretical data. Within our model, H_2 is among the species considered in $\bar{E}_{D,\mathrm{pol}}$ and the abundance of surface H_2 itself is regulated with the help of encounter desorption (Hincelin et al. 2015).

Table 4. Derivation of the H-bond rule: selected molecular E_D on carbonaceous and icy surfaces.[a]

Molecule	$E_{D,\mathrm{pol}}$, K	$E_{D,\mathrm{bare}}$, K	Ref.[b]	Difference *pol-bare*, K
H	650	658	1	-8
H_2	440	542	1	-102
O	1400	1500	2	-100
OH	3500	1360	1	2140
H_2O	5640	2000	1	3640
O_2	1000	1440	1	-440
O_2H	4300	2160	1	2140
H_2O_2	4950	2240	1,3	2710
CO	1300	1100	4	200
CH_3OH	3100	1100	4	2000

[a] The values given in were not used in the model. They illustrate the reasoning for estimating the *pol-bare* values provided in Table 5. [b] 1 – Cuppen & Herbst (2007), 2 – Minissale et al. (2016a), 3 – Cazaux et al. (2010), 4 – Hocuk & Cazaux (2015).

Table 5. The H-bond rule: assumed $E_{D,\mathrm{pol}} - E_{D,\mathrm{bare}}$ for surface species in the model, or the additional binding energy introduced by H-bonds of molecules on ices, compared to molecules on bare carbonaceous grains.

Molecules or functional groups	$E_{D,\mathrm{pol}} - E_{D,\mathrm{bare}}$, K
HF; NH_3; H_2O and H_2O_2	3000
HCl; -OH	2000
-NH; HCN and related	1500
other	0

Finally, we have also implemented a temperature dependence of E_D for water ice, following Hasegawa & Herbst (1993), which is relevant for the warm-up phase of the models. This is described in Appendix A.

2.5. Desorption energy on bare grains

As stated in Section 2.3, our bare grains have a carbonaceous coating. A few other studies have struggled to obtain an assortment of $E_{D,\mathrm{bare}}$ for molecules on carbon because only limited experimental data are available. Cuppen & Herbst (2007) developed such a list for water chemistry, which has been updated by Cazaux et al. (2010). Similar lists have been compiled by Hocuk & Cazaux (2015) and Minissale et al. (2016a); however the latter studies less rigidly stick to carbon and have included E_D values from experiments with silicate or other materials, instead of using estimates for carbon. Some recent experi-

mental data have been published using highly oriented pyrolytic graphite (HOPG), which also show lower bare surface E_D for isolated H-bond forming molecules (Minissale & Dulieu 2014; Doronin et al. 2015; Chaabouni et al. 2018).

The above-mentioned authors employed small reaction networks, which means that our task here is to derive a simple approach with which the differences in $E_{D,\mathrm{pol}}$ on ices and $E_{D,\mathrm{bare}}$ on carbonaceous grains can be attributed to a variety of species. Table 4 summarizes such data from studies that have $E_{D,\mathrm{pol}}$ and $E_{D,\mathrm{bare}}$ based on similar considerations. A striking feature, apparent in the compiled data, is the low $E_{D,\mathrm{bare}}$ values for species that are able to form hydrogen bonds. Another issue is variation of desorption energies for volatile species from H to O_2. No clear pattern can be seen in the latter case.

Table 4 allows us to derive the general approach on devising $E_{D,\mathrm{bare}}$ – subtracting hydrogen bond energy from $E_{D,\mathrm{pol}}$. It also gives an indication on the values that need to be subtracted, which are about ≥2000 K for molecules containing O-H bonds and ≈3000 K for molecules containing two O-H bonds. Naturally, these are lower than often used hydrogen bond energy of about 2800 K because, in absence of H-bonds, other types of molecule-surface bonding are formed instead.

For consistency, we extrapolate the lack of hydrogen bonds on bare grains, or "the H-bond rule" for other molecules containing electronegative atoms associated with H capable of hydrogen bonding, such as nitrogen or halogens. Such a need is underlined by the study of Kakkenpara Suresh et al. (2023), who emphasize the importance of H-bonds for ammonia in circumstellar ices. The qualitative task is now to choose the types of H-bonds that can make a difference in the grain-ice interface. The quantitative task is to evaluate the differences $E_{D,\mathrm{pol}} - E_{D,\mathrm{bare}}$ (or *pol-bare* for short) for the chosen types of H-bonds.

One has to keep in mind that the carbonaceous grain surface likely is quite irregular, seeded with heteroatoms with undivided electron pairs and even an occasional H atom attached to electronegative atoms, such as C in *sp* hybridization. In other words, the carbonaceous surface itself sports some components for weak hydrogen bond formation. From this aspect we infer that only ice molecules that can serve as both electron and proton donors and are able to form the strongest H-bonds can make a difference in the transition from bare surface to icy mantles.

The energy of the OH···O bond in water has been studied most extensively (e.g. Tomoda & Kimura 1983; Ahirwar et al. 2022) with dimer dissociation energies usually in the range of 2300 to 3300 K (Walrafen 2004; Kikuta et al. 2008; Spanu et al. 2008; Sterpone et al. 2008). Such results allow to estimate the effective binding energy difference caused by H-bonding *pol-bare* with an accuracy of about 500 to 1000 K. Some organic molecules, such as alcohols and carboxylic acids are also capable of forming hydrogen bonds via the oxygen atom. Their dissociation energy is in the same range (Andersen et al. 2015). Taking into account the data from Table 4, it seems reasonable to assume $pol - bare = 2000$ K for OH···O bonds. It is encouraging that a 2000 K H-bond energy value also is close to the E_D difference for CH_2OH and CH_3O as obtained by Garrod et al. (2008) via completely different considerations.

Cuppen & Herbst (2007) and Cazaux et al. (2010) E_D compilations indicate that the ability of a molecule to form double H-bonds for H_2O and H_2O_2 does not translate into an *pol-bare* twice as high. Here we take this factor to be 1.5, i.e. *pol-bare*=3000 K for water and hydrogen peroxide.

In the case of ammonia, NH···N hydrogen bonds are only about half as strong, however, OH···N bond energy is similar or even higher than that of OH···O, with dissociation energies of about 3800 K (Yeo & Ford 1994; Kikuta et al. 2008; Ahirwar et al. 2021). Their strength decreases if functional groups are attached to the nitrogen atom (Boryskina et al. 2007; Vallet & Masella 2015). The case of ammonia is further complicated by its protonation in water, not explicitly considered here. As a first approximation, we assume that *pol-bare*=3000 K for ammonia and 1500 K for other compounds containing the N-H bond.

For hydrogen halogenides HF and HCl, dissociation energies for H-bonds with water have been deduced to be about 4300 K and 2700 K by Alkorta & Legon (2023). For hydrogen cyanide, the same authors provide an average value of 2400 K. In line of the above considerations, we assumed *pol-bare* 3000; 2000, and 1500 K for HF, HCl, and HCN, respectively. The latter value was attributed also to the related HNC, HNO and a few other similar molecules.

The *pol-bare* values assumed above are only educated guesses. However, they provide a systemic approach for bare grain E_D, which leaves room for improvements with new data. Table 5 summarizes the hydrogen bond rule applied in this study. The values provided in the table are exact only for completely bare grains, and their effect is reduced proportionally to ice coverage on grains, until the H-bond rule disappears completely, when formal ice thickness reaches 2 MLs, and mobility or evaporation can no longer be affected by molecular interactions with the surface of the refractory grains. This means, for example, that a 1 ML coverage, the *pol-bare* values are only half of their values given in Table 5. Therefore, during the accumulation of the first two ice MLs on a grain with a given size, the H-bond rule for bare grains is gradually replaced by the variable E_D approach designed for icy environments in Section 2.4.

Two MLs as the final threshold for conversion from bare grain effects to the variable E_D in ices was chosen because at 1 ML, all molecules are still affected by their attachment to the bare grain surface, and the effects of the latter cannot be discarded yet. Moreover, the higher 2 ML threshold allows to account for some clustering of molecules on bare grain surface (as indicated by the model of Garrod 2013b), where diffusion, reactions and desorption on patches of bare surface are still possible, even when nominal ice thickness exceeds 1 ML.

2.6. Photodesorption

Photodesorption yield Y_{pd}, molecules per UV photon, has been now measured in a number of experiments. Molecular dynamics simulations reveal that it involves photon absorption at different ice layer depths, direct desorption, photodissociation, trapping or recombination of its products with possible desorption, and "kicking out" neighbours by excited molecules (Andersson et al. 2006; Arasa et al. 2015; van Hemert et al. 2015). The resulting desorption of intact molecules or their fragments depends on surface type (volatile or non-volatile ices, or bare grain, Bertin et al. 2012; Potapov et al. 2019), composition of icy mixtures (Bertin et al. 2016; Carrascosa et al. 2019), possibility for codesorption (Bertin et al. 2013), as well as spectrum of the incident radiation (Fayolle et al. 2011). Experiments show that Y_{pd} depends on ice temperature (Muñoz Caro et al. 2010, 2016), deposition angle (González Díaz et al. 2019), and ice thickness (Öberg et al. 2009b; Sie et al. 2022). Possible presence of atmospheric gases has to be addressed, while a number of experiments irradiate their astrophysical ice analogues by photons with energies below 10–11 eV. This can be a deficiency because important absorption bands may lie at higher energies (Chen et al. 2014; Martín-Doménech et al. 2015; Paardekooper et al. 2016).

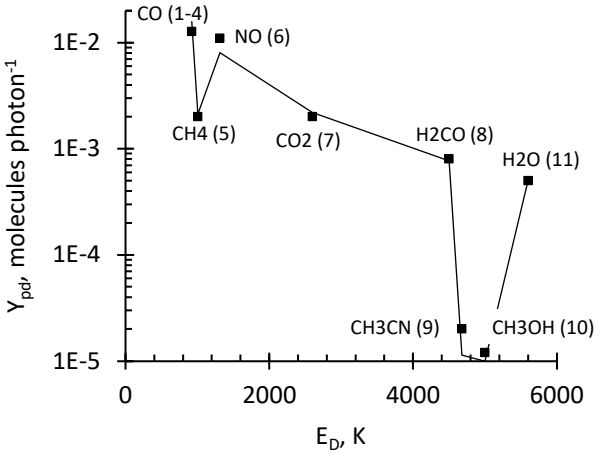

Fig. 1. E_D-dependent photodesorption yield of icy molecules. The line follows Equation 4, while dots indicate experimental data with references in parentheses: 1 – Bertin et al. (2013), 2 – Fayolle et al. (2011), 3 – Fayolle et al. (2013), 4 – Muñoz Caro et al. (2016), 5 – Dupuy et al. (2017a), 6 – Dupuy et al. (2017b), 7 – Fillion et al. (2014), 8 – Féraud et al. (2019), 9 – Basalgète et al. (2021), 10 – Bertin et al. (2016), 11 – Fillion et al. (2022).

The missing wavelengths may induce more efficient desorption as in the case of N_2, or increase the proportion of dissociative desorption, thus reducing the effective Y_{pd} for intact molecules at full λ range.

Several issues also become important, when experimentally obtained Y_{pd} are applied in astrochemical models. First, two types of UV radiation are present – interstellar and cosmic-ray induced photons. Some studies differentiate between the two (Fayolle et al. 2011); the difference is usually within a factor of 2. Second, dissociated fragments may recombine or react with other surface species and undergo chemical desorption (Section 2.7), enhancing the effective yield. This effect is more pronounced for complex molecules that are more easily dissociated.

Considering the above, we compiled set of reliable Y_{pd} data, shown in Figure 1. We used Y_{pd} values for the interstellar radiation field, whenever possible because interstellar photons determine the formation epoch for ices. Moreover, we opted for sources that consider the full 7–13.6 eV range of photons in molecular clouds. Only values for desorption of intact molecules were used because any dissociation fragments have a considerable probability of chemical desorption. Based on the experience from Kalvāns (2015), temperature and spectral influence were considered to be of minor importance and were ignored. Photodesorption from subsurface layers was addressed by allowing photodesorption for molecule depth from up to 4 ice MLs (Andersson & van Dishoeck 2008).

Carbon monoxide CO photodesorption is, perhaps, the most studied and we had the luxury for obtaining and using an average desorption yield $Y_{pd} \approx 10^{-2}$ value from several experimental reports. A number of papers have also studied photodesorption of water H_2O (e.g., Öberg et al. 2009a; Cruz-Diaz et al. 2018; Bulak et al. 2023), and carbon dioxide CO_2, while only Fillion et al. (2014, 2022) considered desorption by photons above 11 eV. Ammonia NH_3 was not included because no ice

Table 6. Chemical desorption efficiency as calculated in the model for watery ices and bare grains, compared to experimental results.

	f_{CD} model		f_{CD} experiment		
Reaction	ice	bare	ice	bare	Ref.[a]
$N + N \rightarrow N_2$	0.44	0.88	0.5	0.7	1
$O + O \rightarrow O_2$	0.36	0.72	…	0.79	2
$O + H \rightarrow OH$	0.20	0.60	0.25	0.5	1
$OH + H \rightarrow H_2O$	0.11	0.50	0.3	0.5	1
$O_2 + H \rightarrow O_2H$	0.00	0.05	…	0.1	3
$CO + H \rightarrow HCO$	0.06	0.13	…	0.1	4
$HCO + H \rightarrow CO + H_2$	0.18	0.36	…	0.4	4
$H_2CO + H \rightarrow HCO + H_2$	0.00	0.00	…	0.1	1
$S + H \rightarrow HS$	0.17	…	≤0.6	…	5
$HS + H \rightarrow H_2S$	0.10	…	≤0.6	…	5

[(a)] 1 – Minissale et al. (2016a), 2 – Minissale & Dulieu (2014), 3 – Dulieu et al. (2013), 4 – Minissale et al. (2016b), 5 – Oba et al. (2018).

desorption data were found for photons with energies exceeding 10.9 eV (Martín-Doménech et al. 2018). Molecular oxygen O_2 largely desorbs via dissociation, and its yield for intact molecules is uncertain (Fayolle et al. 2013). Importantly, usable data are available for some complex organic molecules (COMs). Their intact molecule Y_{pd} is low and chemical desorption of dissociated fragments is the main ejection pathway (Cruz-Diaz et al. 2016; Bulak et al. 2020).

An empirical relation that connects the selected measurements is

$$Y_{pd} = \frac{7076 E_D^{-1.906}}{\eta}, \quad (4)$$

where η is unity for simple molecules with number of atoms $N_{at} < 5$ and $\eta = 10^{N_{at}-4.2}$ for complex molecules with N_{at} of 5 or more atoms. This equation is illustrated with Figure 1. An exception, where Equation 4 was not applied, was created for diatomic monoelemental molecules H_2, N_2 and O_2, which have low yields from pure ices and more efficiently are removed via codesorption (Fayolle et al. 2013). A fixed value $Y_{pd} = 0.0055$ was applied for these molecules (Bertin et al. 2013). We note that because the molecular E_D varies, photodesorption yields typically are lower by about a factor of 0.8 for hyper-volatile molecules and higher for less-volatile ices. In the important and extreme case of water on bare grains ($E_{D,H_2O,bare} = 2600$ K), its $Y_{pd,H_2O,bare} = 0.002$. Such an significantly elevated yield is nonetheless in agreement with experimental data that indicate total (intact and dissociative) $Y_{pd,H_2O,bare}$ of up to 0.5 (Potapov et al. 2019).

2.7. Chemical desorption

Highly-efficient *chemical desorption* of exothermic surface reaction products has been explored experimentally during the last decade (Chaabouni et al. 2012, see also Cazaux et al. 2010). Desorption probability of this process can be up to 90 % (for the OH + H reaction on a silicate surface) and has been quantified and parameterized in further experiments and theoretical works (Dulieu et al. 2013; Minissale & Dulieu 2014; Minissale et al. 2016a; Fredon et al. 2017; Oba et al. 2018; Pantaleone et al. 2020; Molpeceres et al. 2023). This mechanism is especially important for H_2O, which forms via two-step hydrogenation on grain surfaces. Thanks to hydrogenation-dehydrogenation cycles, chemical desorption is relevant also for CO (Minissale et al. 2016b).

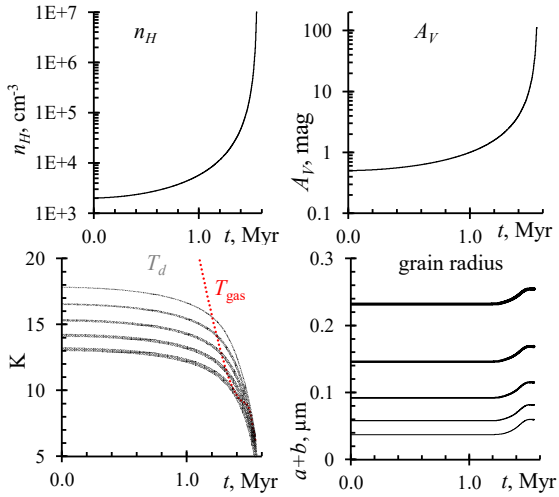

Fig. 2. Density, extinction, temperature, and grain size evolution in the model. For the latter two graphs, thicker curves are for larger grains.

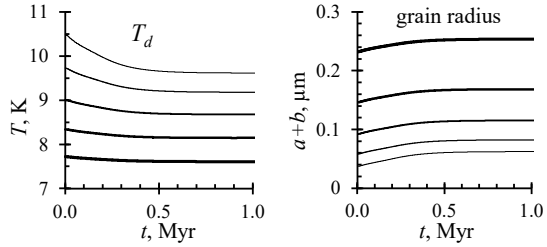

Fig. 3. Grain size and temperature in the pseudo time-dependent cold core Model `const`. Thicker curves are for larger grains, and a is refractory grain radius (constant), while ice mantle thickness b varies with time.

Because chemical desorption is especially effective for water-forming reactions on bare grains, it significantly affects the onset of ice layer formation. This aspect cannot be ignored in chemical modelling focusing on interstellar ices. Thus, we replace the *reactive* desorption of Garrod et al. (2006), previously applied in the Alchemic-Venta model, with the *chemical* desorption method by Minissale et al. (2016a). The variable E_D approach naturally produces different chemical desorption results for different types of surfaces – bare grains, polar ices and non-polar. To account for the less-effective desorption from ices observed in experiments, the chemical desorption efficiency (fraction of desorbed molecules) $f_{\rm CD}$ was modified by a factor of 0.5 for reactions on grains with ice thickness exceeding 1 ML. Table 6 compares experimental $f_{\rm CD}$ values to those used in our model. The application of chemical desorption in concert with our variable-E_D approach is what allows for a realistic and and chemically effective representation of this mechanism, as illustrated by the data in Table 6.

2.8. Collapsing prestellar core macrophysical model

We considered a single point located at the centre of a spherical interstellar molecular core. The cloud model is relatively simple and follows the approach of previous studies. It consists of two main parts. First, the central density n_0 of the core is calculated according to a free-fall collapse scenario (Brown et al. 1988). Hydrodynamical simulations (e.g., Pavlyuchenkov & Zhilkin 2013; Pavlyuchenkov et al. 2015) indicate that actual core collapse can be a few times longer than the free-fall time; thus we delayed the contraction rate by a factor of 0.5. The initial conditions were $n_H = 2000\,{\rm cm}^{-3}$ and $N_H = 1.1 \times 10^{21}\,{\rm cm}^{-2}$, corresponding to initial interstellar extinction $A_V = 0.5$. Second, for each integration step, the spherical (1D) density distribution in the core was obtained with Equation (1) of Kalvāns (2021). This time, core mass was maintained at $2\,{\rm M}_\odot$. Core collapse lasts for another 1.55 Myr until a final density of $1 \times 10^7\,{\rm cm}^{-3}$ is reached. At this point, freeze-out is effectively over and ice composition does not change any more. Figure 2 shows the evolution of physical conditions at the centre of the core.

In the first Results subsection 3.1 we explore variable E_D effects in a pseudo time-dependent Model `const` of a stable, dark molecular core, i.e., with the collapsing core feature switched off. For chemical relaxation, both models were preceded by a 1 Myr long diffuse cloud period, with hydrogen numerical density $n_H = 2000\,{\rm cm}^{-3}$ and interstellar extinction $A_V = 0.5$ mag.

3. Results

Section 2 includes a number of assumptions about desorption energy on interstellar grain surfaces. These assumptions may be closer or farther from reality; however, it is clear that molecule diffusion, evaporation, photodesorption, chemical desorption, and desorption by the H+H surface reaction all depend on E_D to some extent. In turn, E_D is subject to change in different surroundings. Our aim is to clarify if this latter dependence is astrochemically significant and deduce its overall character. To do this, we primarily explore results with a model with a complete set of simulated processes, as described in Section 2 (Model `full`). For illustrating the significance of one or more processes, limited functionality models were used. Table 7 shows that four functionalities of Model `full` were switched off or reduced to rudimentary values: the cloud's macrophysical evolution, the variable-E_D approach, chemical desorption and photodesorption. For context with other models considering multigrain or bulk-ice chemistry, our Table 7 can be compared with Tables 1 and 3 of Pauly & Garrod (2016) and Tables 1 and 7 of Garrod et al. (2022).

We start the description of results with a pseudo-time dependent dense core Models `const` and `const_noEd` (Section 3.1), continue by describing the results of Model `full` and comparing them to Model `noEd`, where the E_D variability is disabled (Section 3.2) and conclude by discussing the importance of photo- and chemical desorption (Section 3.3).

3.1. Cold core model

As an initial test case, we present the basic chemical results for a dense, cold, dark core with constant "classical" physical conditions of $n_H = 2 \times 10^4\,{\rm cm}^{-3}$ and $A_V = 10$ mag. This Model `const` was run for an integration time $t = 1.0$ Myr. During the first few hundred kyr, grain growth occurs up to an ice thickness of 78 MLs on the smallest grains and 66 MLs on the largest grains. Figure 3 shows the change in grain sizes along with the accompanying changes in their temperatures. Gas temperature is constant at $T_{\rm gas} = 8.9$ K, while the cosmic-ray ionization rate $\zeta = 3.2 \times 10^{-17}$ (Section 2.1).

Table 7. Model functionalities and their basic ice chemistry results.

Model	Functionality				Final ice abundance n/n_{H_2}					t of first
	prestellar core	variable E_D	f_{cd}	Y_{pd}	H_2O	CO	CO_2	CH_3OH	NH_3	ice ML, kyr
const		+	$f(E_D)$	$f(E_D)$	1.44E-4	3.17E-5	5.32E-5	1.89E-5	1.88E-5	46
const_noEd			$f(E_D)$	$f(E_D)$	1.43E-4	3.10E-5	5.37E-5	1.85E-5	2.00E-5	5.2
full	+	+	$f(E_D)$	$f(E_D)$	1.28E-4	8.08E-5	4.37E-5	1.26E-5	3.41E-6	1233
noEd	+		$f(E_D)$	$f(E_D)$	1.34E-4	9.13E-5	3.04E-5	1.45E-5	3.57E-6	1176
noPD	+	+	$f(E_D)$	0.001	1.24E-4	7.52E-5	4.89E-5	1.29E-5	3.40E-6	1192
noCD	+	+	0.03	$f(E_D)$	1.03E-4	7.54E-5	4.56E-5	1.47E-5	7.64E-6	1034

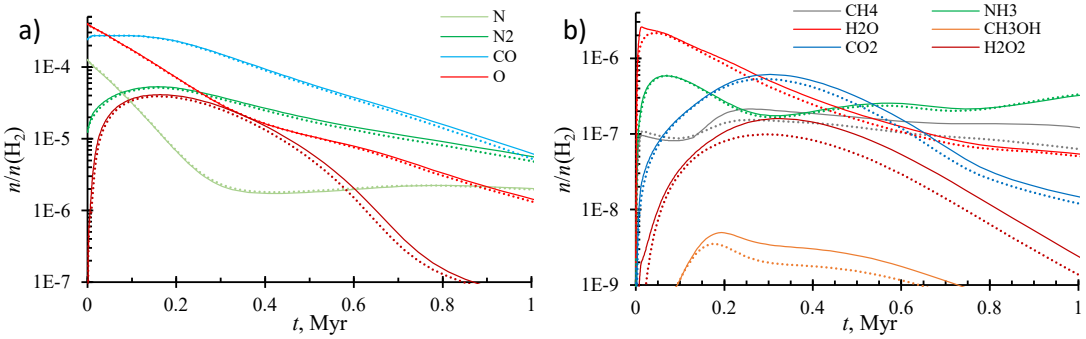

Fig. 4. Calculated gas-phase chemical abundances in the cold core model. Panel (a): relative abundances of major gas-phase species. Panel (b): gas-phase abundances for important molecules that mostly originate from grain surfaces. In both panels, solid lines are for Model const with variable E_D and dotted lines are for Model const_noEd with an unchanging E_D.

Figure 4 shows that the abundances of major gaseous species differ little between Models const and const_noEd with and without the variable-E_D approach, respectively. The easier desorption facilitated by variable E_D is visible in slightly higher gas-phase abundances. The changes are most pronounced to species that are formed via multiple steps on grain surfaces, such as methanol CH_3OH and hydrogen peroxide H_2O_2. Nevertheless, the two simulations produce gas abundances that agree within a factor of 2 for most species and time periods.

Figure 5 shows calculated abundances, relative to water ice, for major icy species for cold core simulations with and without variable E_D. In Model const, 90 % freeze-out is reached at 0.45 Myr, which is later probably by 0.1 Myr or more, compared to comparable multigrain models (Pauly & Garrod 2016; Sipilä et al. 2020). Differences in freeze-out are primarily caused by the consideration or non-consideration of bulk ice, which isolates majority of icy species from most desorption mechanisms, and by the efficient chemical desorption, which acts as delaying function. 99 % freeze-out is reached at 0.74 Myr. For Model const_Ed without differing E_D on bare grains and non-polar ices, the 90 % freeze-out is earlier only by about 0.02 Myr.

A characteristic feature is the low abundance of CO_2 ice for most of the time. The ice ratio CO_2:$H_2O \approx$ 20...30 % is often observed to be similar to that of CO:H_2O (McClure et al. 2023) but here reaches only 8 % at 90 % freeze-out and 16 % at 99 % freeze-out conditions. However, ice CO_2:H_2O continues growing to 23 % at 1 Myr thanks to CO_2 photoproduction via bulk-ice reactions at the expense of H_2O and CO. The cold core model, with its high initial n_H and A_V, is more of a testbed calculation, not able to closely represent real-life scenarios, and underproduction of CO_2 is a typical feature in such models (see Ruffle & Herbst 2001; Bredehöft 2020). The similarity between the abundances of major icy species in Models const and const_noEd indicates that chemistry under rapid freeze-out conditions is regulated mostly by the abundantly adsorbing surface reactants and little affected by E_D variability.

For a review of similar results, albeit without chemical desorption, we refer the reader to Pauly & Garrod (2016), who also employed a model that considers bulk ice, and include a breakdown of ice composition on five grain sizes in their discussion of modelling results. Because we considered larger grains with accordingly lower temperatures, their 5G_T8 models are most relevant. The main difference between our model and that of Pauly & Garrod (2016) is that we consider chemical processing of bulk ice, which slowly increases the abundance of CO_2 ice at the expense of CO and H_2O. Moreover, our model overproduces methanol CH_3OH ice, while their model tends to overproduce methane CH_4 ice, which apparently can be caused by differences in the reaction networks.

3.2. General results

As a context for the discussion that follows, in Figure 6 we show the general chemical results – abundances of major species – for the prestellar core model. With regard to evolution of ices, three periods can be discerned. First is the translucent cloud, dominated by gaseous atomic species and CO, while ice thickness remains below 1 ML. This period lasts for ≈1.2 Myr, until n_H exceeds 10^4 cm^{-3} and $A_V \approx 1.8$ mag. Second is the ice formation period, when core contraction becomes increasingly

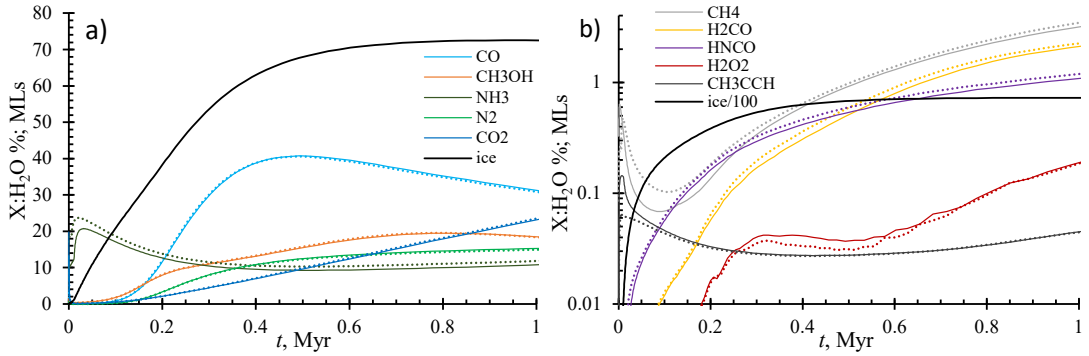

Fig. 5. Calculated chemical abundances icy species in the cold core model. Panel (a): abundances, relative to those of H_2O ice of major icy molecules. The black curve is the average ice thickness $\bar{b}$ on grains, expressed in MLs. Panel (b): selected other abundant ice molecules. For convenience, this time $\bar{b}$ is divided by 100. In both panels, solid lines are for Model `const` with variable E_D and dotted lines are for Model `const_noEd` without the variable-E_D approach.

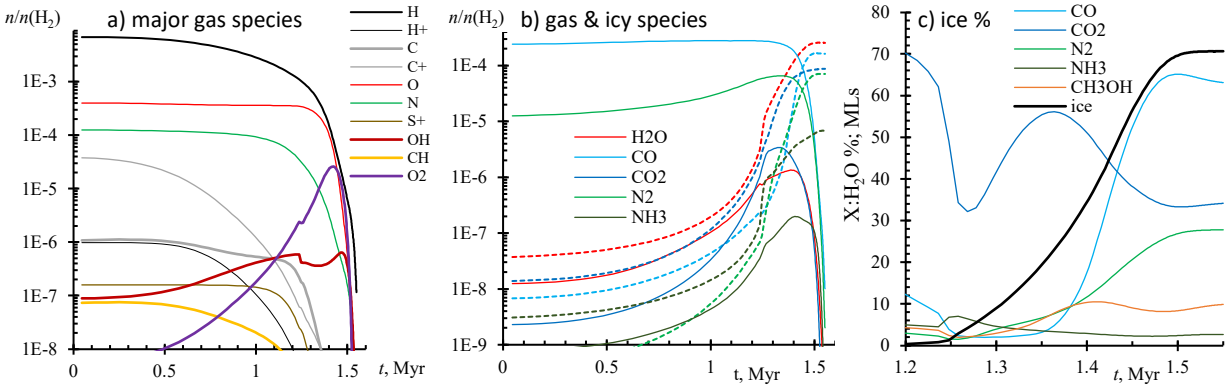

Fig. 6. Overall chemical results for the prestellar core Model `full` with variable E_D and other features enabled. Panel (a): abundance of primary gaseous species relative to that of H_2. Panel (b): species that are abundant in ices, solid lines are for gas-phase, while dashed lines for solid phase abundances, relative to H_2. Panel (c): percentage, relative to H_2O ice, for major icy molecules. The black curve is the average ice thickness $\bar{b}$ on grains.

rapid and up to 99 % of metals accrete on to grains at t=1.5 Myr, $n_H = 3 \times 10^5$ cm^{-3} and $A_V = 14$ mag. Third, during the remaining 25 kyr density increases thirtyfold (with a presumed further collapse towards the first core) with little change in the composition of ices. This period is of limited interest for this study. We continue by describing the translucent and ice formation periods in more detail.

3.2.1. The sub-ML regime in translucent cloud

Adsorbed molecules with average ice thickness below 1 ML likely are present in diffuse and translucent molecular envelopes and thus form a part of sightlines towards prestellar cores. In Model `full`, this is the period when the H-bond E_D rule of bare grains is in effect (Section 2.5). The lack of hydrogen bonding for surface species does not lower their E_D and $E_{\rm diff}$ to significantly promote evaporation or diffusion across the grains (Table 5). However, it is sufficient to elevate chemical desorption and photodesorption yields (Sections 2.6 and 2.7).

Surface chemistry in the translucent cloud is regulated by an interplay between accretion, photodesorption and chemical desorption. Accreted molecules can be desorbed directly by photodesorption or dissociated into fragments. Chemical radicals created on the surface or accreted from the gas react and the product molecules can be desorbed via chemical desorption. Two groups of surface-origin species can be discerned, whose gas abundance is regulated by desorption. First, species like H_2O, NH_3, CH_4, CO_2, CH_3OH reach high gas-phase abundances relative to H_2 (n/n_{H_2}) in excess of 10^{-9}, thanks to photodesorption and rather high surface abundances of $> 10^{-8}$. Second, a variety of species have highly efficient chemical desorption, which, in combination with surface photodissociation, reach gas-phase $n/n_{H_2} > 10^{-12}$. These include, for example, hydrogen peroxide H_2O_2, which is subject to a strong H-bond rule (Table 5) and

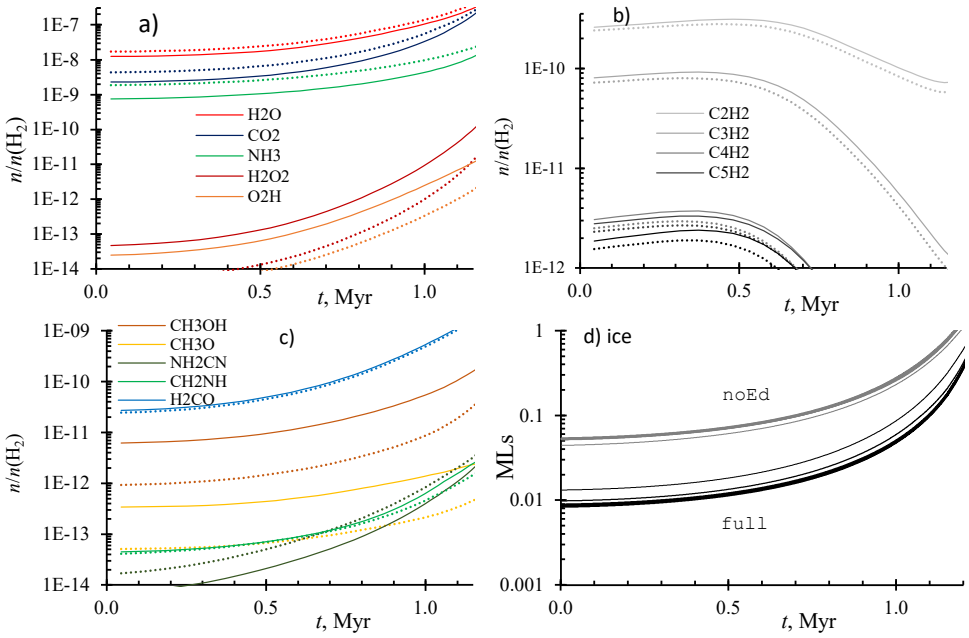

Fig. 7. Variable E_D induced changes in the translucent cloud. Comparison between Models `full` (solid lines) and `noEd` (dotted lines) for selected species including those with gas-phase abundances most affected by E_D changes via the H-bond rule: inorganic in panel (a), carbon chains in panel (b) and other organic in panel (c). Panel (d) shows the growth of ice mantles on the grains, with thinner lines indicating smaller grains. The changes are caused by lack of strong H-bonding on bare grains in Model `full`.

whose abundance changes by about an order of magnitude between Models `full` and `noEd`.

In absolute numbers, most of COMs have gas-phase $n/n_{\rm H_2}$ below 10^{-13} during the translucent period. However, for methanol and a few related compounds, such as CH_3O, abundances exceed 10^{-12} and thus the effect of the lack of H bonds on bare-grains could be observed. Figure 7 illustrates the above discussion and shows also formaldehyde H_2CO, which also has effective chemical desorption. Its E_D is unaffected by the H-bond rule, which means that it has similar translucent cloud abundances for Models `full` and `noEd`. The abundance of CH_3OH and CH_3O is higher by a factor of $\approx$ 5 in Model `full` relative to Model `noEd`; for H_2O_2 and O_2H this factor is 6...10. These factors become lower as time goes by because with the accumulation of ice, the importance of the non-existence of H-bonds on bare grains decreases.

Lack of H bonds on bare grains has a significant effect on overall ice abundances in the sub-ML regime. The release of more H_2O, CO_2 and NH_3 to the gas phase in the Model `full` results in lower by a factor of 2...3 overall adsorbed species' abundances in the variable E_D model. Overall, the lack of H-bonds on bare grains delay the formation of the first ice monolayer by 40 kyr for the smallest and 67 kyr for the largest grains. This delay has an inverse effect on H_2O and CO_2, for which the gas-phase abundances are lower by a factor of 2 because there are less of these molecules on the surface, available for photodesorption. In turn and to a similar extent, a lower gas-phase H_2O abundance positively affects the abundance of carbon chains because H_2O interferes with carbon-chain gas-phase production by reducing the abundance of their building blocks, such as CH, as illustrated with panel (b) of Figure 7. The increase of carbon chain abundance by about a factor of two may not be high but its significance lies in that virtually all unsaturated chains are affected by it.

3.2.2. Ice formation epoch

The ice formation period is when most of ice mass is being accreted onto grains and the ice acquires its initial composition. If the ice is not destroyed (e.g., by falling into the protostar), this composition can be further modified by heating or photoprocessing. Ice formation is characterised by initial formation of a 1 ML thick H_2O-CO_2 layer at the end of the translucent cloud period. It is followed by further accumulation of H_2O and CO_2. When T_d drops below 12 K and CO becomes immobile, CO_2 surface synthesis stalls (Pauly & Garrod 2016) and CO ice accumulates more rapidly, eventually overtaking CO_2 but not H_2O.

In Model `full`, a lower (typically by about 10 %, i.e., *np/pol*$\approx$0.9) varying E_D has two counteracting effects on the abundance of major icy species, compared to Model `noEd` with unchanging E_D. First, a lower diffusion energy for surface CO allows it to remain mobile for longer in Model `full` and thus produce more CO_2 in reactions with O and OH. This effect becomes visible when T_d drops below 14 K. Second, lower $E_{D,\rm CO}$ allows for a more efficient desorption of CO, retaining it longer in the gas-phase, which means that it accretes later at lower T_d, and produces less CO_2. The balance of these two effects depends on the evolution of the modelled cloud and and the choice of model parameters, such as efficiency of various desorption mechanisms, grain size distribution, T_d of grains of different sizes, and, in our model, also the variable E_D approach. Table 7 shows that Model `full` has a CO_2 ice abundance higher by a

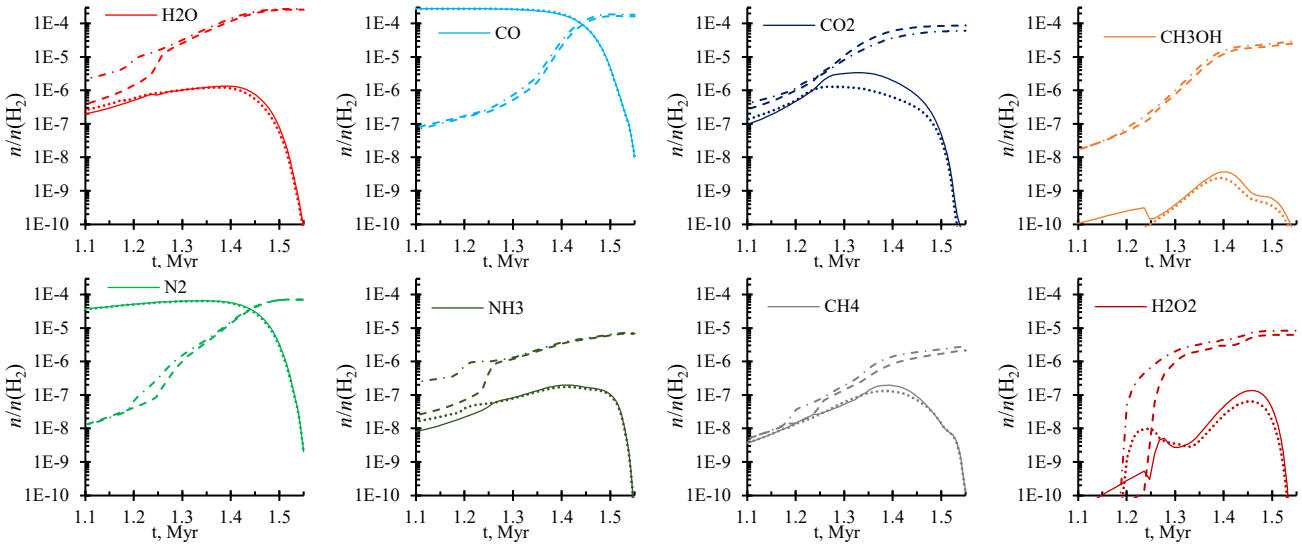

Fig. 8. Variable-E_D induced changes during the ice formation epoch: calculated n/n_{H_2} for species ending up with high ice abundance. Solid and dashed lines are for Model `full` gas-phase and solid species, respectively. Dotted and dash-dotted lines are for gas and solids in Model `noEd`, respectively.

factor of 1.4 than Model `noEd`, i.e., CO_2 production at lower grain temperatures has been more significant.

The overall effect of the addition of varying E_D in the model during the freeze-out stage is higher gas-phase abundances for most species, typically elevated by a factor of 1.5...2 (abundance ratio Model `full`/`noEd`). This occurs thanks to the more efficient chemical and photodesorption. Figure 8 demonstrates several general variable-E_D effects that affect major icy species.

First, the period between 1.19 and 1.26 Myr differs most because the first ice MLs have formed in Model `noEd` but not on the grains of Model `full`. The synthesis of H_2O, NH_3, CO_2 and CH_3OH depends on intermediate radical species with hydrogen bonds (OH, NH, NH_2, CH_2OH). The non-existence of strong H-bonds on bare surface and the resulting efficient chemical desorption (Table 6) is what delays the accumulation of the ice layer in Model `full`.

Second, the lower overall E_D in ices continues to heighten f_{CD} and Y_{pd} for the remainder of cloud evolution, ensuring higher gas-phase abundances for CO, CO_2, N_2 and CH_4in Model `full` . A E_{D,CH_4} lowered by about 100 K means that desorption by the H+H surface reaction heat works on methane in Model `full` but not in Model `noEd`.

The third effect is chemistry in bulk-ices, which is the primary place of synthesis for hydrogen peroxide H_2O_2 and also contributes to the formation of CO_2. Bulk-ice synthesis becomes possible only when >1 MLs of ice have formed. It switches on rapidly and has an immediate effect on H_2O_2 abundances in ice. H_2O_2 appears also in the gas because our model allows photodesorption of bulk ice equal to up to 3 MLs, in addition to 1 surface ML (see Section 2.6).

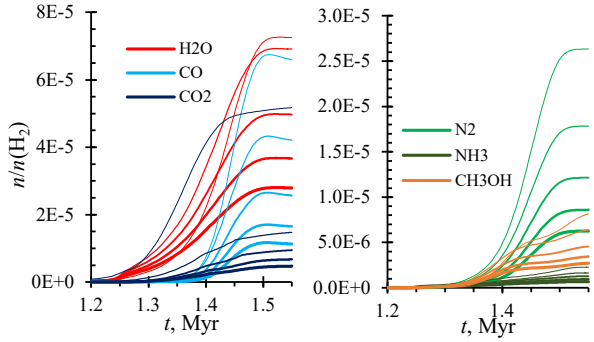

Fig. 9. Evolution of relative abundances for major icy species on grain populations with different sizes.

3.2.3. Distribution of ices

During the ≈50 kyr after the ice formation epoch, residual gas molecules continue to be depleted onto grains. No equilibrium is established because gas density continues to increase rapidly. The final ice composition significantly differs between separate grain size populations. Figure 9 shows that all grains achieve a similar ice thickness in the range of 70...75 MLs. Notably, at the end of the simulation with variable E_D, the smallest grains carry 59 % of all CO_2 and 40 % of CO ice, while other icy species are more evenly distributed between all grain size bins. These results can be explained primarily by the higher temperature of the small grains, which makes CO_2 surface synthesis faster and possible for a longer time in cloud evolution. Because a single CO_2 molecule is formed instead of two molecules

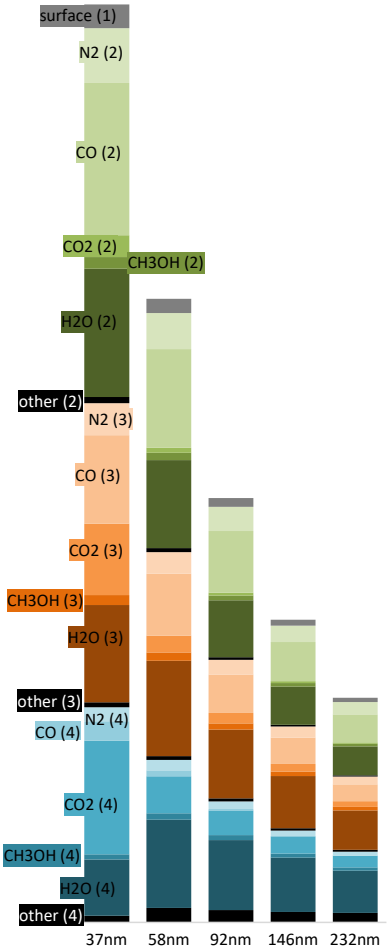

Fig. 10. Distribution of major icy species in different grain size bins, indicated by their size (nm) at final time $t = 1.55$ Myr. The four ice layers are numbered: layer (1) is the surface, while layer (4) is adjacent to the refractory grain core. Species within a single layer are intermixed, they are shown separately here for illustrating their proportions within the layer. Although thickness is similar for all bulk-ice layers for a given grain size, the species in the outer layers are more abundant because the grain has grown. This effect is more pronounced for the smallest grains. Most of the "other" molecules are NH_3 and also CH_4.

of H_2O and CO, ice layer on small-grains is not the thickest (72 MLs at $t = 1.55$ Myr). Concentration of CO_2 on smaller grains occurs also in other multigrain models (Pauly & Garrod 2016; Iqbal & Wakelam 2018).

Figure 10 illustrates the proportions of icy species in the grain size bins at simulation end time t=1.55 Myr. The smallest 0.037 μm carry the highest amount of ice – 37 % of all molecules, compared to only 9 % on the largest 0.232 μm grains. Unlike other simulations, especially two-phase models without bulk-ice layers, such as Iqbal & Wakelam (2018) or Sipilä et al. (2020), cosmic-ray induced desorption has no major effects on the distribution of ices between grains of different sizes.

3.3. Effects of E_D-dependent chemical- and photodesorption

Photodesorption and chemical desorption (Sections 2.6 and 2.7) are two mechanisms whose yields quantitatively depend on E_D and are calculated separately for each surface molecule in each of the five grain size bins in the program. Thus, $f_{\rm CD}$ and $Y_{\rm pd}$ change along with E_D, whose variation is described in Sections 2.4 and 2.5. In other words, chemical desorption and photodesorption are instruments that help communicate the variations in E_D to the gas-ice balance. The efficiency of these mechanisms is anchored in experimental data and often is about an order higher than the safe assumptions applied in astrochemical models during preceding decades.

For comparison with the Model `full`, we ran a simulations with the following changes:

- Model `noPD`, where the E_D-dependent photodesorption yield was replaced with a single constant value $Y_{\rm pd} = 0.001$ for all species;
- Model `noCD`, where the E_D-dependent chemical desorption efficiency was replaced with constant 3 % of all surface reaction products going to the gas phase ($f_{\rm CD} = 0.03$; a simplified version of the reactive desorption by Garrod et al. 2006). This $f_{\rm CD}$ is significantly higher than that used by Garrod et al. (2022).

The above means that in Models `noPD` and `noCD`, photo- or chemical desorption are not disabled, only significantly reduced for simple icy molecules. The fixed $f_{\rm CD}$ and $Y_{\rm pd}$ values are close to previously commonly used desorption parameters. For complex molecules with high E_D and high number of atoms, these fixed desorption efficiencies are actually higher, when compared to the the fully E_D-dependent Model `full`. This is why Model `noCD` shows a peak gas-phase methanol abundance of 1.5×10^{-8} relative to H_2, which is four times higher than that of Model `full` (Figure 11).

In Model `noPD`, the first ice ML is formed at 1.19 Myr on the smallest grains and 1.23 Myr on the largest grains, compared to 1.23...1.24 Myr for Model `full`. Such a moderately earlier ice layer formation is associated with build-up of solid CO_2 and H_2O ices, which have translucent stage abundances higher by factors of 3 and 2 relative to Model `full`, respectively, thanks to their lower $Y_{\rm pd}$ on bare grains. Because CO_2 formation occurs mostly on the smallest grains thanks to their higher T_d, the first ice layer on the small grains in Model `noPD` forms 40 kyr earlier than in Model `full`. For other grain size bins this difference is 16 kyr. Thanks to this advantage, the smallest grains grow the thickest ice, 77 MLs, compared to 65..70 MLs for other grain size bins in Model `noPD`. Once the first layer has formed, ice mass in Model `full` catches up with Model `noPD` within 0.2 Myr because accretion dominates over desorption in the dense core. Table 7 shows that the effect of our E_D-dependent photodesorption approach is moderate, with H_2O:CO:CO_2:CH_3OH:NH_3 final ice abundance ratio being 100:60:39:10:3 in Model `noPD` and 100:63:34:10:3 in Model `full`.

Figure 11 shows that changes introduced by chemical desorption are more pronounced than those of photodesorption. The first ice ML in Model `noCD` forms already at $t = 1.03$ Myr and on the largest, not smallest grains, which is the case in other models. Such a reverse trend can be explained by more efficient hydrogenation of surface O on the lower-temperature large grains along with the fact that H_2O synthesis rate is not diminished by an efficient chemical desorption in Model `noCD`. The abundance of atomic H on grains is in the vicinity of 10^{-12} for all grain size bins in most models. Consequently, the small 0.037 μm grains achieve their first ice ML only at 1.08 Myr and grow the thinnest ice layer of 66 MLs, while for other grain size bins the end thickness is similar at 72...75 MLs.

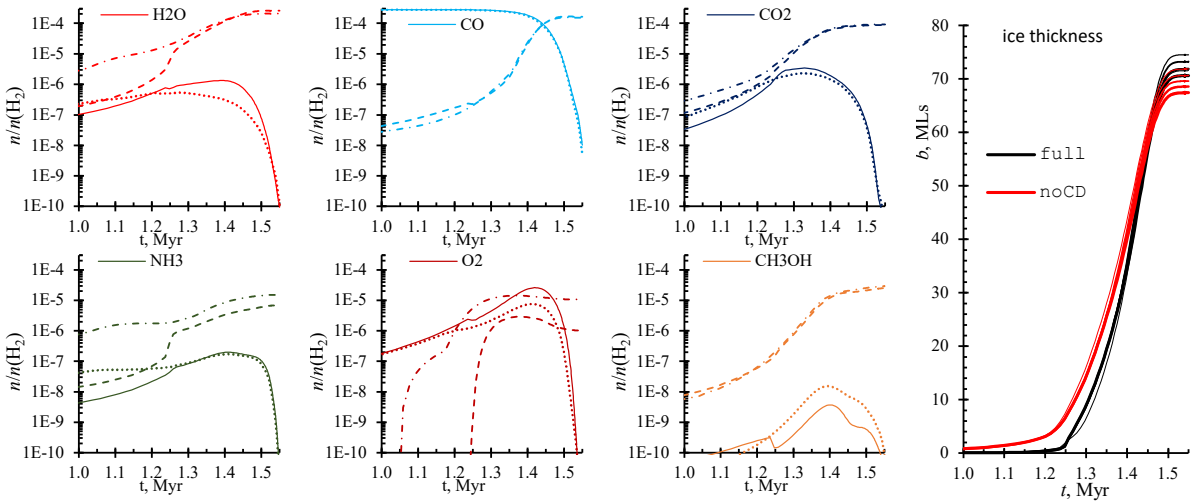

Fig. 11. Ice growth and chemical desorption. Comparison of abundances between Model `full` gas (solid lines) and icy (dashed lines) species with those of Model `noCD` (dotted and dash-dotted lines for gas and ices, respectively). In the ice thickness plot, thicker lines are for larger grains, according to Table 3.

The rapid ice accumulation in Model `noCD` means that the first ice ML forms already at $A_V = 1.1$ mag. In Model `full` this happens only at $A_V = 1.8$ mag. Observable water ice first appears at 3.2 mag extinction along the line-of-sight (Whittet et al. 2001). Our model is too simple to discern, which of the two mechanisms – the high-efficiency chemical desorption (Minissale et al. 2016a) or the low-efficiency reactive desorption (Garrod et al. 2006) – is more consistent with observations because it depends on a number of factors, such as cloud history, its density, irradiation intensity and geometry, and lifetime of the translucent and dark core stages (see Hocuk et al. 2016).

The earlier ice accumulation in Model `noCD` starts at T_d in the range of 12...16 K (a degree higher than in Model `full`) and at about 1.5 times higher interstellar irradiation. Both of these aspects promote surface oxidation of CO, resulting in higher initial CO_2 ice abundances. At later and colder stages, rapid surface synthesis of H_2O wins the competition for surface O and OH because of the inefficiency of the chemical desorption of OH and H_2O in hydrogenation reactions in Model `noCD`.

Oxygen chemistry in Model `noCD` is notably changed by the appearance of surface O_2. The early accumulation of O atoms on relatively warm grains in combination with inefficient hydrogenation allows them to combine with the newly formed O_2 mostly remaining on the surface (see also Pauly & Garrod 2016). Oxygen ice takes up 3.4 % of all oxygen budget, an order of magnitude higher than in Model `full`. Abundant O_2, together with a 60 % higher abundance of H_2O_2, reduces the abundance of water ice by one fifth, which consequently increases the ratios of carbon oxide ices relative to H_2O. The absolute abundances of CO and CO_2 have changed only within 7 % relative to Model `full`.

The H_2O:CO:CO_2:CH_3OH:NH_3:O_2 final ice abundance ratio in Model `noCD` is 100:73:44:10:7:5. This ratio and Figure 11 reveals another important result – the lack of effective chemical desorption allows the formation of ammonia ice with H_2O:NH_3 ratios closer to the ≈10 % value indicated by observations (Boogert et al. 2011). Thus, our results predict that chemical desorption efficiency of nitrogen hydrogenation products NH, NH_2 and NH_3 should be about an order of magnitude lower than indicated by the method of Minissale et al. (2016a).

Chemical desorption also has a significant effect in the pseudo-time dependent model `const`, where, when the Minissale et al. (2016a) chemical desorption is replaced with $f_{CD} = 3$ %, the first full ice ML forms already at $t = 2$ kyr, while 90 % freeze-out is reached about 0.1 Myr earlier.

As far as we know, this is the first published study of a multigrain astrochemical model considering efficient chemical desorption based on the work of Minissale et al. (2016a). While there are few other similar "firsts", combining multiple grain size bins with chemical desorption is important. In multigrain models, grain surface area is higher by about a factor of two, allowing for an earlier accretion of ices. This means accretion at higher gas temperatures of around 20 K, with higher thermal velocities, which makes accretion even more rapid. Small grains increase their surface area with each adsorbed ice ML, leading to a possibility of runaway freeze-out in multigrain models. When chemical desorption is added, it delays the formation of the first ice ML on the bare grain, where it is most effective. Further ice growth continues to be hampered because tens of per cent of hydrogenation reaction products going to the gas phase. Therefore, for multigrain models considering bulk-ice (which means that a major part of ice is isolated from desorption) and efficient chemical desorption, a completely different gas-grain dynamics occurs, which produces results that can be superficially similar to those of much simpler models.

4. Conclusions

The inclusion of chemical desorption (Minissale et al. 2016a) in the multigrain-multilayer gas-surface chemical model turned out to be of major importance. In effect, chemical desorption decreases the rate of icy molecule synthesis, delaying the formation of the ice layer by almost 0.2 Myr, as demonstrated by the comparison of Models `full` and `noCD` in Section 3.3. This aspect is not readily apparent in pseudo-time dependent models,

such as Vasyunin et al. (2017) and Rawlings & Williams (2021) and has been largely missed so far.

Variable E_D has its most visible effect on the abundances of major icy species by increasing the amount of CO_2 at the expense of CO and H_2O. The final calculated relative ice abundances H_2O:CO:CO_2 were 100:63:34, in agreement with heavily shielded dense cores (Whittet et al. 2011; Boogert et al. 2013). The removal of E_D-dependence for one or two molecular-level processes does not disrupt calculated ice composition. The latter finding indicates that the "mysterious" mechanism that regulates the balance between water and carbon oxide ices, sought by authors such as Nejad & Williams (1992); Bergin et al. (1995); Roberts et al. (2007); Kalvāns (2015) is effective and E_D-dependent chemical desorption, photodesorption and desorption by H+H surface reactions, all together. If one of these mechanisms is ineffective in a given cloud core, others can partially offset it, retaining the characteristic $H_2O > [CO \approx CO_2]$ ice abundance sequence. The latter aspect explains the ubiquity of the H_2O:CO:CO_2 ice ratio observations (Gibb et al. 2004; Whittet et al. 2007). Our model is unable to explain a separate problem – the relatively low depletion of CO in interstellar clouds (Leger 1983; Leger et al. 1985; Whittet et al. 2010). Other mechanisms that can contribute to the balance between water and carbon oxides are photodesorption by infrared photons (Williams et al. 1992; Dzegilenko & Herbst 1995; Santos et al. 2023) and cosmic-ray induced desorption (Section 2.1), which was considered but does not have a great effect. An important role is played by grain size distribution, with smaller grains being warmer and more efficient at producing CO_2 ice.

The abundance of solid CH_3OH, in combination with desorption facilitated by lower E_D in our model, is sufficient to explain its observed gas-phase abundance in dark cores (Bacmann et al. 2012; Cernicharo et al. 2012). This is not true for most other COMs, probably due to a limited reaction network. Regarding NH_3, underproduction of ammonia in Model `full` might be explained by an over-effective chemical desorption of hydrogen nitrides in our model. A lower f_{CD} for these molecules is also supported by Sipilä et al. (2019). The chemistry of COMs and nitrogen both merit detailed investigation with this model.

Summarizing, the model combines ten features, which are gradual steps in theoretical (surface) astrochemistry: several grain size bins (1), bulk ice (2) that is chemically active (3) and consists of several separate layers (4), experiment-based estimates for chemical (5) and photodesorption (6), updated estimates for cosmic-ray induced desorption (7) and desorption by surface H atom combination reaction heat (8), a general approach for adjusting E_D on bare grains (9) and a method for estimating E_D in non-polar icy environment (10). While any one of these features may not contribute much and its method can be improved, all together they bring new understanding on how interstellar grain surface chemistry operates, as indicated by previous studies that have investigated many of these features separately (Section 1). Features (6), (9) and (10) are described in a novel way in this study. The above-mentioned delay in ice formation occurs because of combining features (5) and (9), assuming carbonaceous grain surface. We plan to apply this model in further and more specific studies of problems in astrochemistry.

Acknowledgements. This research is funded by the Latvian Science Council grant "Desorption of icy molecules in the interstellar medium (DIMD)", project No. lzp-2021/1-0076. JK thanks Ventspils City Council for support. This research has made use of NASA's Astrophysics Data System.

References

Acharyya, K., Fuchs, G. W., Fraser, H. J., van Dishoeck, E. F., & Linnartz, H. 2007, A&A, 466, 1005
Acharyya, K., Hassel, G. E., & Herbst, E. 2011, ApJ, 732, 73
Ahirwar, M. B., Gurav, N. D., Gadre, S. R., & Deshmukh, M. M. 2022, Physical Chemistry Chemical Physics (Incorporating Faraday Transactions), 24, 15462
Ahirwar, M. B., Patkar, D., Yadav, I., & Deshmukh, M. M. 2021, Physical Chemistry Chemical Physics (Incorporating Faraday Transactions), 23, 17224
Alkorta, I. & Legon, A. 2023, Journal of Physical Chemistry A, 127, 4715
Andersen, J., Heimdal, J., & Wugt Larsen, R. 2015, Physical Chemistry Chemical Physics (Incorporating Faraday Transactions), 17, 23761
Andersson, S., Al-Halabi, A., Kroes, G.-J., & van Dishoeck, E. F. 2006, J. Chem. Phys., 124, 064715
Andersson, S. & van Dishoeck, E. F. 2008, A&A, 491, 907
Arasa, C., Koning, J., Kroes, G.-J., Walsh, C., & van Dishoeck, E. F. 2015, A&A, 575, A121
Bacmann, A., Taquet, V., Faure, A., Kahane, C., & Ceccarelli, C. 2012, A&A, 541, L12
Basalgète, R., Ocaña, A. J., Féraud, G., et al. 2021, ApJ, 922, 213
Bergin, E. A. & Langer, W. D. 1997, ApJ, 486, 316
Bergin, E. A., Langer, W. D., & Goldsmith, P. F. 1995, ApJ, 441, 222
Bertin, M., Fayolle, E. C., Romanzin, C., et al. 2012, Physical Chemistry Chemical Physics (Incorporating Faraday Transactions), 14, 9929
Bertin, M., Fayolle, E. C., Romanzin, C., et al. 2013, ApJ, 779, 120
Bertin, M., Romanzin, C., Doronin, M., et al. 2016, ApJ, 817, L12
Boogert, A. C. A., Chiar, J. E., Knez, C., et al. 2013, ApJ, 777, 73
Boogert, A. C. A., Huard, T. L., Cook, A. M., et al. 2011, ApJ, 729, 92
Boryskina, O. P., Bolbukh, T. V., Semenov, M. A., Gasan, A. I., & Maleev, V. Y. 2007, Journal of Molecular Structure, 827, 1
Bredehöft, J. H. 2020, Frontiers in Astronomy and Space Sciences, 7, 33
Brown, P. D., Charnley, S. B., & Millar, T. J. 1988, MNRAS, 231, 409
Bulak, M., Paardekooper, D. M., Fedoseev, G., & Linnartz, H. 2020, A&A, 636, A32
Bulak, M., Paardekooper, D. M., Fedoseev, G., Samarth, P., & Linnartz, H. 2023, A&A, 677, A99
Carrascosa, H., Hsiao, L. C., Sie, N. E., Muñoz Caro, G. M., & Chen, Y. J. 2019, MNRAS, 486, 1985
Cazaux, S., Cobut, V., Marseille, M., Spaans, M., & Caselli, P. 2010, A&A, 522, A74
Cernicharo, J., Marcelino, N., Roueff, E., et al. 2012, ApJ, 759, L43
Chaabouni, H., Diana, S., Nguyen, T., & Dulieu, F. 2018, A&A, 612, A47
Chaabouni, H., Minissale, M., Manicò, G., et al. 2012, J. Chem. Phys., 137, 234706
Chang, Q., Cuppen, H. M., & Herbst, E. 2007, A&A, 469, 973
Chang, Q. & Herbst, E. 2014, ApJ, 787, 135
Chang, Q. & Herbst, E. 2016, ApJ, 819, 145
Chen, L.-F., Chang, Q., & Xi, H.-W. 2018, MNRAS, 479, 2988
Chen, Y. J., Chuang, K. J., Muñoz Caro, G. M., et al. 2014, ApJ, 781, 15
Collings, M. P., Anderson, M. A., Chen, R., et al. 2004, MNRAS, 354, 1133
Cruz-Diaz, G. A., Martín-Doménech, R., Moreno, E., Muñoz Caro, G. M., & Chen, Y.-J. 2018, MNRAS, 474, 3080
Cruz-Diaz, G. A., Martín-Doménech, R., Muñoz Caro, G. M., & Chen, Y. J. 2016, A&A, 592, A68
Cuppen, H. M. & Herbst, E. 2007, ApJ, 668, 294
Das, A., Sil, M., Gorai, P., Chakrabarti, S. K., & Loison, J. C. 2018, ApJS, 237, 9
Doronin, M., Bertin, M., Michaut, X., Philippe, L., & Fillion, J. H. 2015, J. Chem. Phys., 143, 084703
Duley, W. W. & Williams, D. A. 1993, MNRAS, 260, 37
Dulieu, F., Congiu, E., Noble, J., et al. 2013, Scientific Reports, 3, 1338
Dupuy, R., Bertin, M., Féraud, G., et al. 2017a, A&A, 603, A61
Dupuy, R., Féraud, G., Bertin, M., et al. 2017b, A&A, 606, L9
Dzegilenko, F. & Herbst, E. 1995, ApJ, 443, L81
Fayolle, E. C., Balfe, J., Loomis, R., et al. 2016, ApJ, 816, L28
Fayolle, E. C., Bertin, M., Romanzin, C., et al. 2011, ApJ, 739, L36
Fayolle, E. C., Bertin, M., Romanzin, C., et al. 2013, A&A, 556, A122
Féraud, G., Bertin, M., Romanzin, C., et al. 2019, ACS Earth and Space Chemistry, 3, 1135
Fillion, J.-H., Dupuy, R., Féraud, G., et al. 2022, ACS Earth and Space Chemistry, 6, 100
Fillion, J.-H., Fayolle, E. C., Michaut, X., et al. 2014, Faraday Discussions, 168, 533
Flynn, G. J. 2020, in Oxford Research Encyclopedia of Planetary Science (Oxford University Press), 143
Fredon, A., Lamberts, T., & Cuppen, H. M. 2017, ApJ, 849, 125
Furuya, K., Drozdovskaya, M. N., Visser, R., et al. 2017, A&A, 599, A40
Garrod, R., Park, I. H., Caselli, P., & Herbst, E. 2006, Faraday Discussions, 133, 51

Garrod, R. T. 2013a, ApJ, 765, 60
Garrod, R. T. 2013b, ApJ, 778, 158
Garrod, R. T. & Herbst, E. 2006, A&A, 457, 927
Garrod, R. T., Jin, M., Matis, K. A., et al. 2022, ApJS, 259, 1
Garrod, R. T. & Pauly, T. 2011, ApJ, 735, 15
Garrod, R. T., Weaver, S. L. W., & Herbst, E. 2008, ApJ, 682, 283
Gavino, S., Dutrey, A., Wakelam, V., et al. 2021, A&A, 654, A65
Ge, J. X., He, J. H., & Li, A. 2016, MNRAS, 460, L50
Gibb, E. L., Whittet, D. C. B., Boogert, A. C. A., & Tielens, A. G. G. M. 2004, ApJS, 151, 35
González Díaz, C., Carrascosa de Lucas, H., Aparicio, S., et al. 2019, MNRAS, 486, 5519
Grassi, T., Bovino, S., Caselli, P., et al. 2020, A&A, 643, A155
Hasegawa, T. I. & Herbst, E. 1993a, MNRAS, 261, 83
Hasegawa, T. I. & Herbst, E. 1993b, MNRAS, 263, 589
He, J., Acharyya, K., & Vidali, G. 2016, ApJ, 825, 89
He, J., Emtiaz, S., & Vidali, G. 2018, ApJ, 863, 156
Hincelin, U., Chang, Q., & Herbst, E. 2015, A&A, 574, A24
Hocuk, S. & Cazaux, S. 2015, A&A, 576, A49
Hocuk, S., Cazaux, S., Spaans, M., & Caselli, P. 2016, MNRAS, 456, 2586
Hocuk, S., Szűcs, L., Caselli, P., et al. 2017, A&A, 604, A58
Iqbal, W. & Wakelam, V. 2018, A&A, 615, A20
Ivlev, A. V., Padovani, M., Galli, D., & Caselli, P. 2015, ApJ, 812, 135
Jin, M. & Garrod, R. T. 2020, ApJS, 249, 26
Johnson, D. G., Blitz, M. A., & Seakins, P. W. 2000, Physical Chemistry Chemical Physics (Incorporating Faraday Transactions), 2, 2549
Kakkenpara Suresh, S., Dulieu, F., Vitorino, J., & Caselli, P. 2023, arXiv e-prints, arXiv:2311.18619
Kalvāns, J. 2015, ApJ, 803, 52
Kalvāns, J. 2018, MNRAS, 478, 2753
Kalvāns, J. & Kalnin, J. R. 2019, MNRAS, 486, 2050
Kalvāns, J. & Shmeld, I. 2010, A&A, 521, A37
Kalvāns, J. 2015, ApJ, 806, 196
Kalvāns, J. 2021, ApJ, 910, 54
Kalvāns, J. & Kalnin, J. R. 2022, ApJS, 263, 5
Kalvāns, J. & Silsbee, K. 2022, MNRAS, 515, 785
Kikuta, Y., Ishimoto, T., & Nagashima, U. 2008, Chemical Physics, 354, 218
Leger, A. 1983, A&A, 123, 271
Leger, A., Jura, M., & Omont, A. 1985, A&A, 144, 147
Martín-Doménech, R., Cruz-Díaz, G. A., & Muñoz Caro, G. M. 2018, MNRAS, 473, 2575
Martín-Doménech, R., Manzano-Santamaría, J., Muñoz Caro, G. M., et al. 2015, A&A, 584, A14
Martín-Doménech, R., Muñoz Caro, G. M., Bueno, J., & Goesmann, F. 2014, A&A, 564, A8
Mathis, J. S., Rumpl, W., & Nordsieck, K. H. 1977, ApJ, 217, 425
McClure, M. K., Rocha, W. R. M., Pontoppidan, K. M., et al. 2023, Nature Astronomy, 7, 431
McElroy, D., Walsh, C., Markwick, A. J., et al. 2013, A&A, 550, A36
Minissale, M. & Dulieu, F. 2014, J. Chem. Phys., 141, 014304
Minissale, M., Dulieu, F., Cazaux, S., & Hocuk, S. 2016a, A&A, 585, A24
Minissale, M., Moudens, A., Baouche, S., Chaabouni, H., & Dulieu, F. 2016b, MNRAS, 458, 2953
Molpeceres, G., Zaverkin, V., Furuya, K., Aikawa, Y., & Kästner, J. 2023, A&A, 673, A51
Muñoz Caro, G. M., Chen, Y. J., Aparicio, S., et al. 2016, A&A, 589, A19
Muñoz Caro, G. M., Jiménez-Escobar, A., Martín-Gago, J. Á., et al. 2010, A&A, 522, A108
Nejad, L. A. M. & Williams, D. A. 1992, MNRAS, 255, 441
Noble, J. A., Congiu, E., Dulieu, F., & Fraser, H. J. 2012, MNRAS, 421, 768
Oba, Y., Tomaru, T., Lamberts, T., Kouchi, A., & Watanabe, N. 2018, Nature Astronomy, 2, 228
Öberg, K. I., Linnartz, H., Visser, R., & van Dishoeck, E. F. 2009a, ApJ, 693, 1209
Öberg, K. I., van Broekhuizen, F., Fraser, H. J., et al. 2005, ApJ, 621, L33
Öberg, K. I., van Dishoeck, E. F., & Linnartz, H. 2009b, A&A, 496, 281
Paardekooper, D. M., Fedoseev, G., Riedo, A., & Linnartz, H. 2016, A&A, 596, A72
Padovani, M., Galli, D., & Glassgold, A. E. 2009, A&A, 501, 619
Pantaleone, S., Enrique-Romero, J., Ceccarelli, C., et al. 2021, ApJ, 917, 49
Pantaleone, S., Enrique-Romero, J., Ceccarelli, C., et al. 2020, ApJ, 897, 56
Pauly, T. & Garrod, R. T. 2016, ApJ, 817, 146
Pauly, T. & Garrod, R. T. 2018, ApJ, 854, 13
Pavlyuchenkov, Y. N. & Zhilkin, A. G. 2013, Astronomy Reports, 57, 641
Pavlyuchenkov, Y. N., Zhilkin, A. G., Vorobyov, E. I., & Fateeva, A. M. 2015, Astronomy Reports, 59, 133
Penteado, E. M., Walsh, C., & Cuppen, H. M. 2017, ApJ, 844, 71
Potapov, A., Jäger, C., & Henning, T. 2019, ApJ, 880, 12
Rawlings, J. M. C. 2022, MNRAS, 517, 3804
Rawlings, J. M. C. & Williams, D. A. 2021, MNRAS, 500, 5117
Roberts, J. F., Rawlings, J. M. C., Viti, S., & Williams, D. A. 2007, MNRAS, 382, 733
Ruffle, D. P. & Herbst, E. 2001, MNRAS, 324, 1054
Sandford, S. A. & Allamandola, L. J. 1988, Icarus, 76, 201
Santos, J. C., Chuang, K. J., Schrauwen, J. G. M., et al. 2023, A&A, 672, A112
Semenov, D., Hersant, F., Wakelam, V., et al. 2010, A&A, 522, A42
Shingledecker, C. N., Vasyunin, A., Herbst, E., & Caselli, P. 2019, ApJ, 876, 140
Shinoda, T. 1969, Bulletin of the Chemical Society of Japan, 42, 2815
Sie, N.-E., Cho, Y.-T., Huang, C.-H., et al. 2022, ApJ, 938, 48
Silsbee, K., Caselli, P., & Ivlev, A. V. 2021, MNRAS, 507, 6205
Silsbee, K., Ivlev, A. V., Sipilä, O., Caselli, P., & Zhao, B. 2020, A&A, 641, A39
Sipilä, O., Caselli, P., Redaelli, E., Juvela, M., & Bizzocchi, L. 2019, MNRAS, 487, 1269
Sipilä, O., Zhao, B., & Caselli, P. 2020, A&A, 640, A94
Spanu, L., Sterpone, F., Ferraro, L., Sorella, S., & Guidoni, L. 2008, in APS March Meeting Abstracts, APS Meeting Abstracts, Q26.006
Sterpone, F., Spanu, L., Ferraro, L., Sorella, S., & Guidoni, L. 2008, arXiv e-prints, arXiv:0806.4169
Takahashi, J. & Williams, D. A. 2000, MNRAS, 314, 273
Taquet, V., Ceccarelli, C., & Kahane, C. 2012, A&A, 538, A42
Taquet, V., Charnley, S. B., & Sipilä, O. 2014, ApJ, 791, 1
Terwisscha van Scheltinga, J., Ligterink, N. F. W., Bosman, A. D., Hogerheijde, M. R., & Linnartz, H. 2022, A&A, 666, A35
Thi, W.-F., Woitke, P., & Kamp, I. 2010, MNRAS, 407, 232
Tielens, A. G. G. M. & Hagen, W. 1982, A&A, 114, 245
Tielens, A. G. G. M., Tokunaga, A. T., Geballe, T. R., & Baas, F. 1991, ApJ, 381, 181
Tomoda, S. & Kimura, K. 1983, Chemical Physics Letters, 102, 560
Vallet, V. & Masella, M. 2015, Chemical Physics Letters, 618, 168
van Hemert, M. C., Takahashi, J., & van Dishoeck, E. F. 2015, Journal of Physical Chemistry A, 119, 6354
Vasyunin, A. I., Caselli, P., Dulieu, F., & Jiménez-Serra, I. 2017, ApJ, 842, 33
Vidali, G., Ihm, G., Kim, H.-Y., & Cole, M. W. 1991, Surface Science Reports, 12, 135
Wakelam, V., Loison, J. C., Mereau, R., & Ruaud, M. 2017, Molecular Astrophysics, 6, 22
Walrafen, G. E. 2004, in American Institute of Physics Conference Series, Vol. 716, Portable Synchrotron Light Sources and Advanced Applications: International Symposium on Portable Synchrotron Light Sources and Advanced Applications, ed. H. Yamada, N. Mochizuki-Oda, & M. Sasaki, 45–48
Whittet, D. C. B., Cook, A. M., Herbst, E., Chiar, J. E., & Shenoy, S. S. 2011, ApJ, 742, 28
Whittet, D. C. B., Gerakines, P. A., Hough, J. H., & Shenoy, S. S. 2001, ApJ, 547, 872
Whittet, D. C. B., Goldsmith, P. F., & Pineda, J. L. 2010, ApJ, 720, 259
Whittet, D. C. B., Shenoy, S. S., Bergin, E. A., et al. 2007, ApJ, 655, 332
Willacy, K., Williams, D. A., & Duley, W. W. 1994, MNRAS, 267, 949
Williams, D. A., Hartquist, T. W., & Whittet, D. C. B. 1992, MNRAS, 258, 599
Yeo, G. A. & Ford, T. A. 1994, Spectrochimica Acta Part A: Molecular Spectroscopy, 50, 5
Zhao, B., Caselli, P., & Li, Z.-Y. 2018, MNRAS, 478, 2723
Zuo, W., Li, A., & Zhao, G. 2021, ApJS, 252, 22